Cryoelectron tomography reveals periodic material at the inner side of subpellicular microtubules in apicomplexan parasites

Marek Cyrklaff,[1] Mikhail Kudryashev,[2] Andrew Leis,[1] Kevin Leonard,[3] Wolfgang Baumeister,[1] Robert Menard,[4] Markus Meissner,[2] and Friedrich Frischknecht[2]

[1]Department of Molecular Structural Biology, Max Planck Institute for Biochemistry, 82152, Martinsried, Germany
[2]Department of Parasitology, Hygiene Institute, University of Heidelberg Medical School, 69120 Heidelberg, Germany
[3]European Molecular Biology Laboratory-European Bioinformatics Institute, Wellcome Trust Genome Campus, Cambridge CB10 1SD, UK
[4]Malaria Biology and Genetics Unit, Institut Pasteur, 75015 Paris, France

Microtubules are dynamic cytoskeletal structures important for cell division, polarity, and motility and are therefore major targets for anticancer and antiparasite drugs. In the invasive forms of apicomplexan parasites, which are highly polarized and often motile cells, exceptionally stable subpellicular microtubules determine the shape of the parasite, and serve as tracks for vesicle transport. We used cryoelectron tomography to image cytoplasmic structures in three dimensions within intact, rapidly frozen *Plasmodium* sporozoites. This approach revealed microtubule walls that are extended at the luminal side by an additional 3 nm compared to microtubules of mammalian cells. Fourier analysis revealed an 8-nm longitudinal periodicity of the luminal constituent, suggesting the presence of a molecule interacting with tubulin dimers. In silico generation and analysis of microtubule models confirmed this unexpected topology. Microtubules from extracted sporozoites and *Toxoplasma gondii* tachyzoites showed a similar density distribution, suggesting that the putative protein is conserved among Apicomplexa and serves to stabilize microtubules.

CORRESPONDENCE
Marek Cyrklaff:
cyrklaff@biochem.mpg.de
OR
Friedrich Frischknecht:
freddy.frischknecht@
med.uni-heidelberg.de

Plasmodium parasites are the causative agents of malaria. *Plasmodium* sporozoites are transmitted to the mammalian host via the bite of an infected mosquito (1). The sporozoites can migrate from the entry point within the skin, enter the bloodstream, and eventually invade hepatocytes, where they differentiate into blood cell–invading forms (2, 3). Apicomplexan parasites are highly polarized cells with an unusual cytoskeleton (4). Their cytoplasmic microtubules are very stable and resistant to most microtubule depolymerizing drugs (4, 5). These microtubules are located below the parasite pellicle, originate at the apical polar rings, which are structures of unknown composition and function, and terminate near the parasite nucleus (4). Whereas in a particular parasitic form the number and spatial distribution of subpellicular microtubules is relatively fixed, both differ between species and the parasite stages in the life cycle (4). Sporozoites of *Plasmodium berghei*, which is a rodent malaria parasite, contain 15–16 microtubules arranged circumferentially on a polar ring, and collectively enclose a cone-shaped cage (6) (Fig. 1, A and B). The microtubules are evenly spaced over two-thirds of the cell circumference, while a single one is positioned in the third sector (6) (Fig. 1, A and B). Accumulated in this cage underneath the apical polar rings are several organelles (micronemes, rhoptries, and dense granules), which play distinct roles during host cell infection (7). This part of the sporozoite is referred to as the "apical complex," a defining feature of the phylum Apicomplexa. To gain insights into the structure and distribution of the microtubules, we studied *P. berghei* sporozoites with cryoelectron tomography (Cryo-ET), which combines the potential of three-dimensional imaging with a true-to-life preservation of biological samples (8, 9). *P. berghei* sporozoites, which are typically ~10 μm long and <1 μm thick, are ideal objects for studies with Cryo-ET in whole-mount preparations. We focused on the microtubule cytoskeleton, where we detected and analyzed regularly distributed luminal components.

The Journal of Experimental Medicine

RESULTS AND DISCUSSION

Cryo-ET tomography of *Plasmodium* sporozoite microtubules in situ

Microtubules are readily discernible in electron tomograms (10–12) (Fig. 1), and detailed analysis is facilitated by their composition of repeating subunits (tubulin dimers) and associated proteins that typically follow this pattern. Microtubules in *P. berghei* sporozoites interacted side-on, rather than end-on, with the polar ring (13) (Fig. 1, A–C). Whereas at one side of a sporozoite the microtubules ended at the polar ring, at the opposite side they extended beyond the inclined polar ring (Fig. 1 C), suggesting that the interaction was flexible. The majority of the microtubule ends at the polar ring (frequently referred to as minus ends; reference 14) were flared (46 out of 51 investigated; Fig. 1 C), and only ~10% were blunt-ended and capped, resembling γ-tubulin minus ends in higher eukaryotes (15). The appearance of the microtubule ends was the same, irrespective of whether they were located at the polar ring or extended beyond it (Fig. 1 C). Interestingly, most of the opposite (or distal) ends of these microtubules (referred to as plus ends) usually appeared open-ended, with no visible flare (Fig. 1 D). This may suggest that most sporozoite microtubules are in a state of disassembly (16), although most published data show that subpellicular microtubules are stable (4, 5, 17). To investigate this apparent discrepancy, we examined microtubules in more detail.

The subpellicular microtubules appear morphologically homogeneous in the tomograms (Fig. 1, A–D). The outer diameter of microtubules measured 26 ± 1.2 nm (n = 80), which is typical for microtubules of other eukaryotes (18). However, the sporozoite microtubules showed an electron lucent central volume of only ~12 nm in diameter, compared with the usual 18-nm diam in microtubules from other eukaryotic cells or from in vitro–polymerized microtubules (Fig. 1 E). As a consequence, the walls of sporozoite microtubules appeared ~3 nm thicker than those from controls, suggesting a unique microtubule topology.

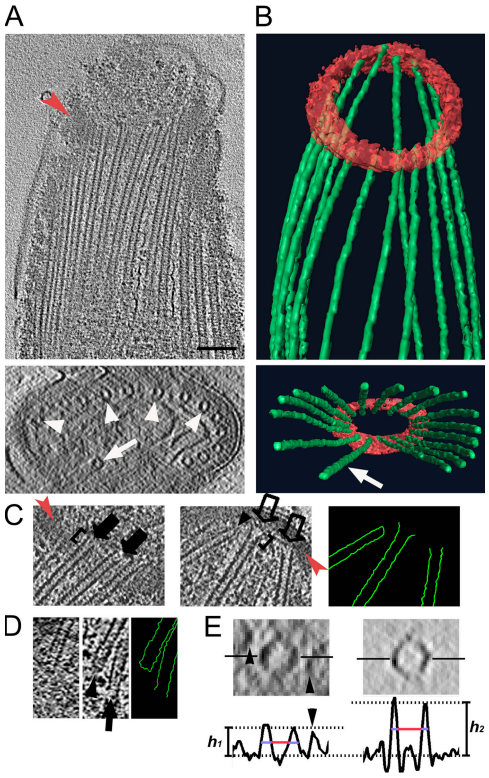

Figure 1. Subpellicular microtubules of *P. berghei* sporozoites. (A) Longitudinal (top) and cross (bottom) slices through a tomographic reconstruction from the apical part of a *Plasmodium* sporozoite revealing subpellicular microtubules. Red arrowhead, polar ring; white arrowheads, circumferentially arranged microtubules; arrow, the lone microtubule. (B) Volume-rendered representations of the microtubules (green) and the polar ring (red) from the same tomogram. (C) Microtubules interact side-on (left, black arrows) and end-on (middle, open arrows) with the proximal polar ring (red arrowheads). The microtubule ends are mostly flared ([ ]). A capped microtubule is marked by an arrowhead. (right) The outlines of the microtubules shown in the middle image. (D) Ends of microtubules close to the nucleus appear open (arrow) or closed (arrowhead). (right) Microtubule outlines from the middle image. (E) Cross-sections of microtubules from a sporozoite (left) and from in vitro polymerization (right). Arrowheads indicate neighboring microtubules. Density distributions along the horizontal lines are displayed in the graphs. Dotted lines indicate background and maximal heights (h1 and h2). Microtubule widths (blue-red lines) were determined at half heights. Red line, diameter of lumen; blue lines, microtubule walls. Bar, 100 nm (for A–D).

Analysis of sporozoite microtubules

Fourier transforms generated from the tomograms of microtubules revealed strong layer lines at 1/8 nm^{-1} (Fig. 2 A and Fig. S1, available at http://www.jem.org/cgi/content/full/jem.20062405/DC1), indicating the presence of a well-defined, periodic motif repeating in the longitudinal direction and corresponding to the frequency of tubulin dimers (19). From the digital volumes of computationally unbent microtubules, we dissected, Fourier transformed, and analyzed subvolumes as indicated in Fig. 2 (B and C). The material generating the 1/8 nm^{-1} intensity was present in the inner space of the microtubule and absent from both the wall and the microtubule outer surface (Fig. 2, A–D).

To investigate the distribution of this luminal component, we masked volumes using cylinder-like or tubelike masks (Fig. 2 E). By iteratively increasing the respective radii R1 and R2 of the masks, we could selectively pass information in distinct volumes, and investigate the intensities of the 1/8 nm^{-1} signal in the corresponding Fourier transforms. The plots of the relative intensities over increasing R1 and R2 showed that most of the 1/8 nm^{-1} signal, indeed, conformed to volumes located within the lumen of the microtubule (Fig. 2, F–H). We then applied a band-pass filter to the Fourier spectra of the unbent microtubules, to pass the signal of all the layer lines with multiples of 1/4 nm^{-1}. On back- projections, the filtered volumes showed that the luminal densities align tightly at the microtubule wall (Fig. 2 I).

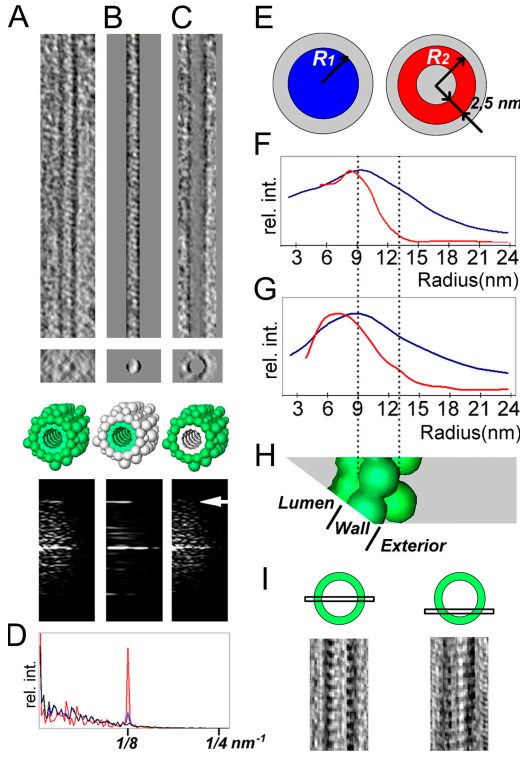

Figure 2. Analysis of sporozoite microtubules. (A) Front and top views of a computationally unbent microtubule. Green, subvolume used in Fourier analysis. The Fourier transform shows a predominant signal at the 1/8 nm^{-1} longitudinal repeat. (B) From the microtubule in A, a central luminal cylinder with 9-nm radius (green in diagram) was analyzed. Note the strong 1/8 nm^{-1} signal in the Fourier transform. (C) The same microtubule masked opposite to B, i.e., excluding the 9 nm lumen, shows no signal at 1/8 nm^{-1} in Fourier transform. Arrow marks 1/8 nm^{-1} for all Fourier transforms. (D) Intensity distribution plots of Fourier transforms from A (blue), B (red), and C (black) projected in the equatorial direction. Rel int, relative intensity. (E–H) Analysis of the 1/8 nm^{-1} intensity in Fourier transforms similar to D, but in relation to microtubule radius. (E) Schematic illustration of two types of incremental subvolume extractions used in F and G. (left) Cylindrical volumes (blue) with increasing radii R1 were extracted from a microtubule (gray). (right) Hollow tubular volumes (red) with increasing radii R2 were extracted. The width of the mask was a constant 2.5 nm. (F) Radial distribution of the 1/8 nm^{-1} intensities over increasing R1 (blue cylinder) and R2 (red tube) measured for the microtubule in A, as described in E. Graphs were scaled to equal maxima. (G) Mean intensities from four microtubules that were analyzed as in F. (H) A diagram exemplifying radial density distribution in a *Plasmodium* microtubule radially aligned with F and G with dotted lines (microtubule wall). (I) *Plasmodium* microtubule after band-pass–filtering, including the equator, 1/4, 1/8, 1/16 and 1/32 nm^{-1} layer lines, and back-transformation. The planes of sectioning are indicated in the schematic drawings.

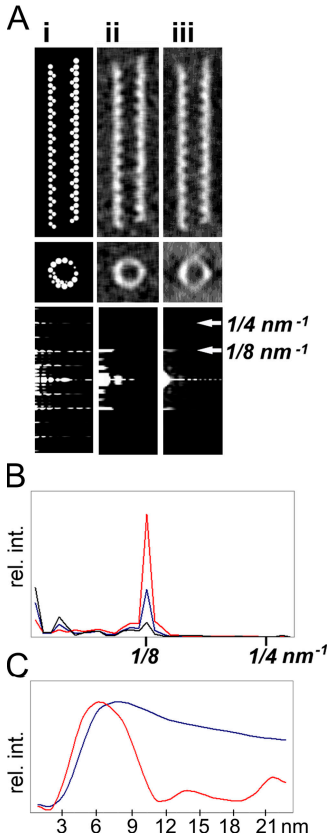

Figure 3. Analysis of in silico–generated microtubule models. (A, i) Microtubule model created in silico containing 8-nm periodicity inside the lumen. (ii) Model with noise added. (iii) Tomographic reconstruction of the model. (B) Analysis as in Fig. 2 D of the in silico reconstruction from A, iii. Projected Fourier transforms: blue, entire volume; red, microtubule lumen within a 9-nm radius; black, volumes outside of the 9-nm radius. (C) Relative intensity distribution of the 1/8 nm^{-1} signal in analogy to Fig. 2 F.

Modeling microtubules

To assess data accuracy and to identify any possible image processing artifacts, we created two model systems that were processed in virtually the same way as the original datasets. First, we computationally generated a series of projection images from either the original tomograms of microtubules or from rotationally averaged microtubules around their longitudinal axes, and then we back-projected them to new volumes. Both were analyzed using the same constraints as the original datasets. Subvolume analyses indicated a similar spatial distribution of the 1/8 nm^{-1} signal for both models (Fig. S2, available at http://www.jem.org/cgi/content/full/jem.20062405/DC1). Thus, the 8-nm periodic densities within the lumen of sporozoite microtubules could not be attributed to distortions inherent in tomographic structure analysis, such as the missing wedge of data or smearing of densities (8).

Second, we created and analyzed several microtubule models entirely in silico. The principal model, which was composed of a 13-protofilament helical lattice, was additionally decorated with 2.9-nm densities at the luminal side, with 8-nm longitudinal spacing (Fig. 3). We applied noise to this model with values that are typical for EM images of whole cells, generated a series of 2D projections from the incrementally tilted volume, and computed tomograms from this tilt series using the standard weighted back-projection procedure (Fig. 3 A and Fig. S3, available at http://www.jem.org/cgi/content/full/jem.20062405/DC1). The 1/8 nm^{-1} signal

in the reconstructed models was distributed similarly to that in the microtubules from the original tomograms (Fig. 3, B and C; and Fig. S3 C). The tomograms of microtubule models differently oriented to the tilt axis revealed the same radial distribution of the 1/8 nm^{-1} signal, but their intensities varied over different angles (Fig. S4). Therefore, we only used microtubules with the same orientation toward the tilt axes for comparative analyses.

In an alternative model, the 2.9-nm densities were placed in 8-nm periodicity at the outer face of the microtubule model wall (Fig. S5, available at http://www.jem.org/cgi/content/full/jem.20062405/DC1). This allowed us to test whether or not the distortions inherent to tomographic reconstruction could be responsible for a flawed mass displacement and erroneous appearance of the densities in the microtubule lumen. In reconstructions, the 1/8 nm^{-1} signal was only detected in subvolumes localized outside the lumen of 9 nm radius (Fig. S5 C). Together, these analyses confirmed that the 8-nm periodic material is a constituent of the lumen of subpellicular microtubules and not an effect of data recording or processing artifacts.

Analysis of microtubules from different species and isolated cytoskeletons

Having confirmed the luminal location of the densities, we next investigated if such a distribution was specific for *Plasmodium* or could be found in microtubules from other species. Using the same electron microscope settings and image acquisition conditions, we recorded tilt series of various intact cells of eukaryotic origin, as well as microtubules nucleated in vitro from pig brain tubulin. Resulting tomograms typically showed 4-nm-thick microtubule walls, and the absence of additional densities, as well as an absence of 8-nm periodicities along the lattice (Fig. S6, A–C, available at http://www.jem.org/cgi/content/full/jem.20062405/DC1). Notably, the lumen of neuronal microtubules was also filled with periodically distributed densities, but these occupied the central volume of the lumen (10).

To examine microtubules from species related to *Plasmodium*, we imaged cytoskeletons extracted from *Toxoplasma* tachyzoites by cell lysis, as the intact forms are too thick for imaging in EM. We also recorded tomograms of lysed *Plasmodium* sporozoites. These microtubules showed a similar distribution of luminal densities to that found in the intact sporozoites (Fig. 4, A, B, E, and G). Intact (or completely folded) microtubules containing the luminal densities were present in tomograms of *Toxoplasma* tachyzoites that were extracted at room temperature with 5% Triton for 30 min, followed by phosphate-buffered saline adjusted to 2 M NaCl for 60 min before freezing (Fig. 4, C, D, F, and G), indicating that the uncommon microtubule topology is preserved in Apicomplexa and that these microtubules are exceptionally stable (4, 5, 13). When additionally treated with the microtubule depolymerizing drug oryzalin, microtubules in *Toxoplasma* extracts appeared shorter, and were occasionally ruptured. The newly exposed ends within the cracks were connected to each other, and the intact stretches between ruptures revealed the characteristic topology of the 8-nm luminal periodic densities (Fig. S7, available at http://www.jem.org/cgi/content/full/jem.20062405/DC1).

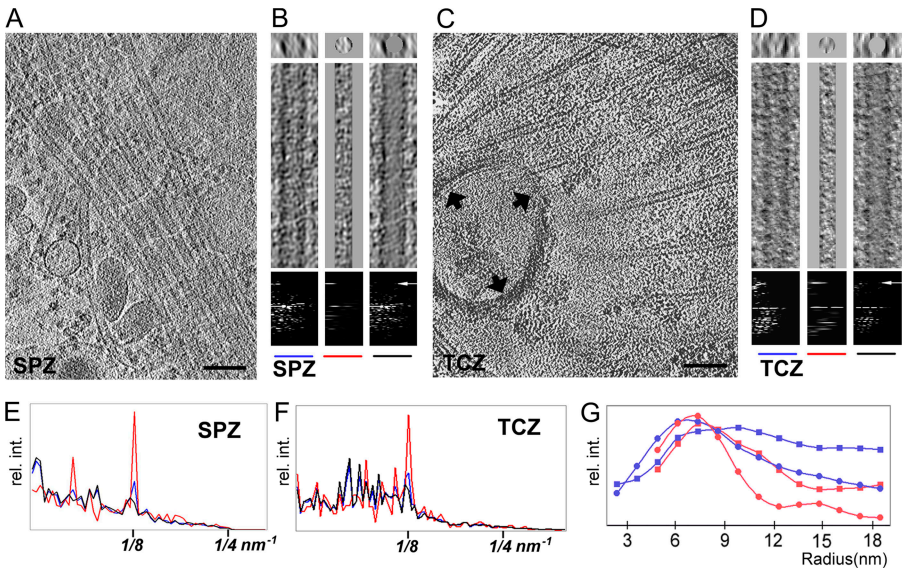

Figure 4. Analysis of microtubules extracted from *P. berghei* sporozoites and *T. gondii* tachyzoites. (A) Microtubules from a lysed sporozoite (SPZ). (B) Subvolume analysis as in Fig. 2 (A–C) of an unbent microtubule from A. White arrows in Fourier transforms in B and D indicate 1/8 nm^{-1}. (C) Microtubules from lysed tachyzoite (TCZ). Note the presence of a polar ring (arrows). (D) Analysis of an unbent tachyzoite microtubule as in B. (E and F) Relative intensity distributions in the Fourier transforms of microtubules were calculated for sporozoites (SPZ) and tachyzoites (TCZ), as in Fig. 2 D; entire volumes (blue), the lumens (red), and the microtubules excluding lumens (black). (G) Radial distribution of the 1/8 nm^{-1} signal within microtubules from B and D, calculated as in Fig. 2 (E and F); microtubules from sporozoite (circles) and tachyzoite (squares). Bars, 100 nm.

Microtubules in strongly bent parasites

During transmission, motile sporozoites often undergo sharp turns, and they occasionally squeeze through tight barriers (3). This indicates that the subpellicular microtubules, apart from being stable, should also be highly elastic. Fig. 5 and Video 1 (available at http://www.jem.org/cgi/content/full/jem.20062405/DC1) illustrate the bending that can be readily observed for motile sporozoites in vitro and in situ. As expected, examination of bent sporozoites with Cryo-ET showed that the microtubules followed the curvature of the cells (Fig. S8). In a particularly striking example, we found a sporozoite tightly bent over the edge of a hole in the EM grid carbon support (Fig. 5, C–F), which was similar to what can be observed in vivo when sporozoites enter or exit blood vessels (3). Strikingly, all microtubules were intact and showed 180 degree turns with radii as small as 86 nm (Fig. 5, D–F).

A novel molecule binding at the lumen of the microtubules

Concerning the nature of the extended wall, it could be hypothesized that the luminal densities are caused by either large tubulin subunits or specific microtubule-associated proteins. Both α- and β-tubulin from *Plasmodium* and *Toxoplasma* are highly similar to tubulins from all other species. They differ mainly within the 15 C-terminal amino acids, which is too small to detect using whole-cell tomography. Therefore, we favor the hypothesis that an unconventional microtubule-associated molecule (probably a protein) binds to tubulin from the luminal side and stabilizes these microtubules. As a rule, microtubules depolymerize rapidly at noncapped ends (20). The subpellicular microtubules attached to the polar ring were mostly open-flared, exposing the uncapped ends, but were evidently not depolymerizing (4). Detailed inspection of these microtubule ends indicated that the densities within the microtubule lumen appeared only at the sites where the microtubules were completely folded, but did not appear on the flared protofilaments (Fig. 1 C). We thus speculate that the microtubules might be in a state of "suspended depolymerization" in which the flared open ends are prone to depolymerization, but microtubules remain stabilized, possibly because of the presence of a luminal binding partner. The dissociation of this molecule, or an alteration of its functional state, could thus lead to the gradual depolymerization of subpellicular microtubules that is observed when sporozoites successfully invade a host cell (21).

The association or interaction of molecules with the inner side of a microtubule has been demonstrated for taxol and its derivatives (22) and discussed for the microtubule-associated protein tau (23, 24). Interestingly, tau accumulates at sites of microtubule bending, suggesting that it helps in preventing microtubule rupture (25). This could also be the role of the putative luminal protein in Apicomplexa, as a 1/8-nm^{-1} layer line could also be observed in the highly bent tubulin fibers of the toxoplasma conoid (19). Sporozoites undergo extreme bends during gliding and transmission, when they squeeze through or maneuver around obstacles (3) (Fig. 5 and Video 1). This suggests that sporozoites contain a highly

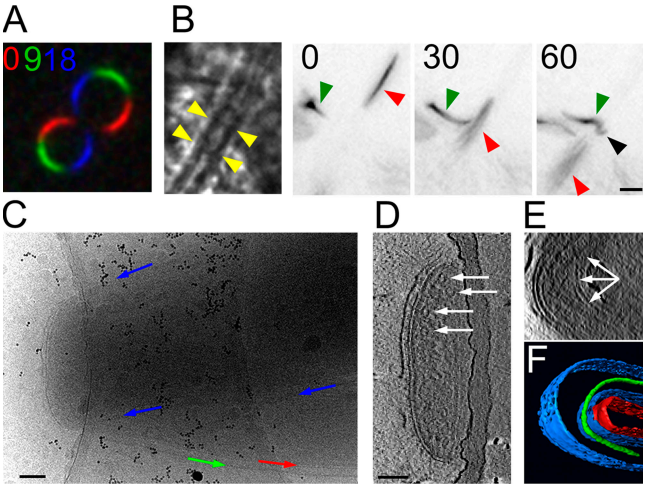

Figure 5. Sporozoite bending and microtubule organization. (A) Pseudocolored time-lapse recording of two gliding sporozoites reveals the near-perfect circular movement of the parasites in vitro in the absence of obstacles. (B) Movement of two sporozoites within an isolated salivary gland. (left) Chitinized walls of the salivary duct are indicated by yellow arrowheads. (right) One sporozoite (red arrowheads) moves within the salivary duct. The other sporozoite (green arrowheads) moves within the salivary gland tissue. Note the deformation of the sporozoite upon encountering the rigid wall (black arrowhead). Time is indicated in seconds in A and B. (C) Projection image of a sporozoite strongly bent in the vertical axis over the edge of the carbon support. The sporozoite is tightly constricted at the site of the bend. Arrows indicate the sporozoite plasma membrane at one side of the carbon support (blue arrow), at the other side (green arrow), and at the inner membrane complex (red arrow). (D) Cross-section through the tomogram of the area shown in C. The microtubules are circular (arrows). (E) Side view of the same reconstruction. Arrows depict the curvature of a microtubule bent with a radius of 86 nm. (F) The same view as in E, with selected features highlighted; plasma membrane (blue), microtubule (green), and carbon support (red). For clarity, only one microtubule is highlighted. Bars: (A and B) 5 μm; (C–F) 100 nm.

elastic cytoskeleton, which might be essential for successful transmission of the parasite. Indeed, strongly bent microtubules in frozen sporozoites did not show any signs of breakage, despite exceeding the curvature that microtubules of higher eukaryotes can accomplish before breaking (26). Thus, it might be possible that the stabilization of subpellicular microtubules in these parasites has evolved as a mechanism to protect them from breaking when the parasites penetrate tissue barriers.

Microtubules in neuronal processes, flagella, and some other tissues frequently exhibit central or luminal densities (10, 11). In neurons, the distribution of luminal densities suggests that these molecules are unlikely to interfere with microtubule dynamics (10). In contrast, the luminally associated densities found in flagella appear to be capable of inhibiting complete microtubule depolymerization, thus suggesting a role in microtubule stabilization (11). The finding of similar luminal densities in flagella from sea urchin sperm (11, 12), *Chlamydomonas reinhardtii* (11), and trypanosomes (27) suggests

that the function of these proteins is conserved in a wide range of organisms. It is tempting to speculate on a stabilizing function of these proteins, as they occur in microtubules, which need to be both elastic and strong. Currently, one can only speculate if the proteins of Apicomplexa and the axonemes of flagella are related and have a similar function, as further research is needed to identify these proteins. Our data suggest that whatever the role of these proteins, it appears to be restricted to rigid microtubule assemblies that do not undergo treadmilling.

MATERIALS AND METHODS

Cryo-ET and image analysis. Isolated parasites in cell culture medium were transferred onto holey EM carbon grids, incubated for 20–40 min, and rapidly frozen after removal of excess of liquid (28). Frozen-hydrated grids were mounted in a cryoholder (model 626; Gatan) and investigated in an electron microscope (CM 300; FEI), equipped with field emission gun and Gatan post column energy filter (accelerating voltage, 300 keV; objective lens spherical aberration coefficient: 2.8 mm). The tilt series of low-dose images (60–100 of each area, with a cumulative dose of ~4,000 electrons/nm^2), filtered at zero energy loss, were recorded on a 2k × 2k pixel charge-coupled device camera (Gatan), at a magnification of 51,000 (0.68 nm/pixel) and an objective lens defocus of between −5 and −15 μm (the lowest defocus dataset had the first zero of CTF at 1/3 nm^{-1}). The same defocus was used when reconstructions were compared with each other. A total of 21 tomographic reconstructions were calculated by weighted back-projection using the "EM-image processing package." Some reconstructions were noise-reduced using nonlinear anisotropic diffusion. Visualization, volume rendering, and segmentation were performed using the Amira package (TGS Europe).

The subvolumes (256^3 voxels) containing differently oriented microtubules were extracted from the cryotomograms of sporozoites, and aligned parallel to the y axis of the subtomograms. The pixel size was 1.36 nm (1× binning). Some microtubules were unbent using a TOM package plug-in.

For Fig. 2 I, the Fourier volumes of computationally unbent microtubules were bandpass filtered using masks that included only the signal along the equator and the multiples of 1/4 nm^{-1} layer planes. The thickness of the masks (L) was defined as described in supplemental methods. After back-projection, the denoised microtubules were sectioned longitudinally at different planes to demonstrate the topology of the luminal material.

The amplitudes of three-dimensional Fourier spectra were projected onto one-dimensional plots, and background normalized. We compared the 1/8 nm^{-1} signal in the lumen of microtubules within the radius of 9 nm, with the remaining volumes comprising tubulin wall and adjacent cytoplasm. Radial distributions of the 8-nm signal were plotted by masking the selected volumes in radial increments of 1 pixel (1.36 nm; see Supplemental materials and methods, available at http://www.jem.org/cgi/content/full/jem.20062405/DC1).

Online supplemental material. Figs. S1–S8 provide data showing the maximum achievable resolution in tomograms from intact sporozoites (Fig. S1), an extensive description of the modeling approaches (Figs. S2–S5), and data from control preparations (Fig. S6–S8). The supplementary video demonstrates the elasticity of sporozoites. Methods describing in detail the modelling approaches are described in the Supplemental materials and methods. Online supplemental material is available at http://www.jem.org/cgi/content/full/jem.20062405/DC1.

We thank Rogerio Amino, Ken Downing, Francois Dubremetz, Vladan Lucic, Richard McIntosh, Sylvia Münter, Stuart Ralph, and Isabelle Tardieux for many helpful comments and discussions. We thank Beatrice Martin, Diana Scheppan, and Manuela Breinich for their technical assistance.

The work was supported by a grant from the Pasteur Institute Grand Programme Horizontal Anopheles, a long-term fellowship from the Human Frontier Science Program to F. Frischknecht, and grants from the Bundesministerium für Bildung und Forschung (BioFuture) to M. Messner and F. Frischknecht.

The authors have no conflicting financial interests.

Submitted: 15 November 2006
Accepted: 24 April 2007

REFERENCES

1. Amino, R., R. Menard, and F. Frischknecht. 2005. In vivo imaging of malaria parasites–recent advances and future directions. *Curr. Opin. Microbiol.* 8:407–414.
2. Prudencio, M., A. Rodriguez, and M.M. Mota. 2006. The silent path to thousands of merozoites: the Plasmodium liver stage. *Nat. Rev. Microbiol.* 4:849–856.
3. Amino, R., S. Thiberge, B. Martin, S. Celli, S. Shorte, F. Frischknecht, and R. Menard. 2006. Quantitative imaging of Plasmodium transmission from mosquito to mammal. *Nat. Med.* 12:220–224.
4. Morrissette, N.S., and L.D. Sibley. 2002. Cytoskeleton of apicomplexan parasites. *Microbiol. Mol. Biol. Rev.* 66:21–38.
5. Morrissette, N.S., A. Mitra, D. Sept, and L.D. Sibley. 2004. Dinitroanilines bind {alpha}-tubulin to disrupt microtubules. *Mol. Biol. Cell.* 15:1960–1968.
6. Vanderberg, J., J. Rhodin, and M. Yoeli. 1967. Electron microscopic and histochemical studies of sporozoite formation in *Plasmodium berghei*. *J. Protozool.* 14:82–103.
7. Dubremetz, J.F., N. Garcia-Reguet, V. Conseil, and M.N. Fourmaux. 1998. Apical organelles and host-cell invasion by Apicomplexa. *Int. J. Parasitol.* 28:1007–1013.
8. Lucic, V., F. Forster, and W. Baumeister. 2005. Structural studies by electron tomography: from cells to molecules. *Annu. Rev. Biochem.* 74:833–865.
9. McIntosh, R., D. Nicastro, and D. Mastronarde. 2005. New views of cells in 3D: an introduction to electron tomography. *Trends Cell Biol.* 15:43–51.
10. Garvalov, B.K., B. Zuber, C. Bouchet-Marquis, M. Kudryashev, M. Gruska, M. Beck, A. Leis, F. Frischknecht, F. Bradke, W. Baumeister, et al. 2006. Luminal particles within cellular microtubules. *J. Cell Biol.* 174:759–765.
11. Nicastro, D., C. Schwartz, J. Pierson, R. Gaudette, M.E. Porter, and J.R. McIntosh. 2006. The molecular architecture of axonemes revealed by cryoelectron tomography. *Science.* 313:944–948.
12. Sui, H., and K.H. Downing. 2006. Molecular architecture of axonemal microtubule doublets revealed by cryo-electron tomography. *Nature.* 442:475–478.
13. Russell, D.G., and R.G. Burns. 1984. The polar ring of coccidian sporozoites: a unique microtubule-organizing centre. *J. Cell Sci.* 65: 193–207.
14. Fowler, R.E., A.M. Smith, J. Whitehorn, I.T. Williams, L.H. Bannister, and G.H. Mitchell. 2001. Microtubule associated motor proteins of *Plasmodium falciparum* merozoites. *Mol. Biochem. Parasitol.* 117:187–200.
15. Moritz, M., M.B. Braunfeld, V. Guenebaut, J. Heuser, and D.A. Agard. 2000. Structure of the gamma-tubulin ring complex: a template for microtubule nucleation. *Nat. Cell Biol.* 2:365–370.
16. Mandelkow, E.M., E. Mandelkow, and R.A. Milligan. 1991. Microtubule dynamics and microtubule caps: a time-resolved cryo-electron microscopy study. *J. Cell Biol.* 114:977–991.
17. Morrissette, N.S., and L.D. Sibley. 2002. Disruption of microtubules uncouples budding and nuclear division in Toxoplasma gondii. *J. Cell Sci.* 115:1017–1025.
18. Mandelkow, E.M., and E. Mandelkow. 1985. Unstained microtubules studied by cryo-electron microscopy. Substructure, supertwist and disassembly. *J. Mol. Biol.* 181:123–135.
19. Hu, K., D.S. Roos, and J.M. Murray. 2002. A novel polymer of tubulin forms the conoid of *Toxoplasma gondii*. *J. Cell Biol.* 156:1039–1050.
20. Rodionov, V.I., and G.G. Borisy. 1997. Microtubule treadmilling in vivo. *Science.* 275:215–218.

21. Meis, J.F., J.P. Verhave, A. Brouwer, and J.H. Meuwissen. 1985. Electron microscopic studies on the interaction of rat Kupffer cells and *Plasmodium berghei* sporozoites. *Z. Parasitenkd.* 71:473–483.
22. Nogales, E., M. Whittaker, R.A. Milligan, and K.H. Downing. 1999. High-resolution model of the microtubule. *Cell.* 96:79–88.
23. Kar, S., J. Fan, M.J. Smith, M. Goedert, and L.A. Amos. 2003. Repeat motifs of tau bind to the insides of microtubules in the absence of taxol. *EMBO J.* 22:70–77.
24. Santarella, R.A., G. Skiniotis, K.N. Goldie, P. Tittmann, H. Gross, E.M. Mandelkow, E. Mandelkow, and A. Hoenger. 2004. Surface-decoration of microtubules by human tau. *J. Mol. Biol.* 339:539–553.
25. Samsonov, A., J.Z. Yu, M. Rasenick, and S.V. Popov. 2004. Tau interaction with microtubules in vivo. *J. Cell Sci.* 117:6129–6141.
26. Gupton, S.L., W.C. Salmon, and C.M. Waterman-Storer. 2002. Converging populations of F-actin promote breakage of associated microtubules to spatially regulate microtubule turnover in migrating cells. *Curr. Biol.* 12:1891–1899.
27. Vaughan, S., M. Shaw, and K. Gull. 2006. A post-assembly structural modification to the lumen of flagellar microtubule doublets. *Curr. Biol.* 16:R449–R450.
28. Adrian, M., J. Dubochet, J. Lepault, and A.W. McDowall. 1984. Cryo-electron microscopy of viruses. *Nature.* 308:32–36.